Impact of alternative divertor configuration on plasma detachment: pure Deuterium simulations with SolEdge2D-EIRENE edge transport code for HL-2M scenario

R Mao, N. Fedorczak, G. Ciraolo, H. Bufferand, Y. Marandet, J. Bucalossi, P. Tamain, E. Serre, G y Zheng, J. Li

To cite this version:

R Mao, N. Fedorczak, G. Ciraolo, H. Bufferand, Y. Marandet, et al.. Impact of alternative divertor configuration on plasma detachment: pure Deuterium simulations with SolEdge2D-EIRENE edge transport code for HL-2M scenario. Nuclear Fusion, 2019. hal-02370418

HAL Id: hal-02370418
https://hal.science/hal-02370418

Submitted on 19 Nov 2019

Impact of alternative divertor configuration on plasma detachment: pure Deuterium simulations with SolEdge2D-EIRENE edge transport code for HL-2M scenario

R Mao[1], N Fedorczak[1], G Ciraolo[1], H Bufferand[1], Y. Marandet[2], J. Bucalossi[1], P. Tamain[1], E. Serre[3], G.Y Zheng[4], J.X Li[4]
[1] CEA, IRFM, F-13108 Saint Paul-lez-Durance, France
[2] Aix Marseille Univ., CNRS, PIIM, Marseille, France
[3]Aix Marseille Univ., CNRS, Centrale Marseille, M2P2, Marseille, France
[4] SWIP, Chengdu, China

Abstract

The SOLEDGE-EIRENE edge plasma code provides solutions for particle & energy transport in the plasma edge within complex and realistic 2D geometries [1]. In this work, divertor detachment is simulated on the HL-2M alternative magnetic configurations in pure Deuterium plasma. Starting from typical HL-2M low single-null (SN) configuration, the snowflake plus (SF+) and snowflake minus (SF-) configurations have been investigated. Detachment of the outer target is studied in these configurations during plasma density ramps controlled by a fueling source, at constant input power and constant radial transport coefficients. Some typical characteristics of detachment, like threshold, depth and upstream window of detachment are investigated. In the three geometries, detachment onset and evolution with upstream plasma density is characterized by the gradual displacement of a radiation front from the outer target to the main X-point, as observed in experiments. It is found that, whatever the detachment in terms of particle, momentum or power dissipation, the detachment threshold is dominated primarily by the geometrical structure of divertor plate and it does not exhibit dependence on the magnetic configuration of the diverted plasma volume. In particular, the parallel connection length in the divertor is not found to affect the detachment threshold, in contrast with simple expectations from the 2-point model, but in agreement with experimental findings.

Keywords: detachment, alternative magnetic geometry, edge transport simulation

1. Introduction

Power exhaust is one of the challenging issues that the next generation of magnetized fusion devices (ITER, DEMO) will face. As an illustration, in ITER-size devices it is expected that the conducted power flowing from the core region into the thin boundary layer called Scrape Off Layer (SOL) will be in the range of more than 100MW [2, 3]. From simple considerations this implies that the plasma heat fluxes impacting the divertor target plates are expected to be into the range of 50 MW/m^2, assuming conservative wetted areas and no dissipation in the diverted plasma volume; far more than engineering limits of 10 MW/m^2. For this reason, an important effort is currently ongoing in order to find scenarios able to maximize power dissipation mechanisms into the divertor region, as well as possible alternative magnetic configurations able to maximize the plasma-wetted area, reducing the peak heat load.

The divertor configuration allows substantial temperature gradients along the magnetic field line from upstream SOL to the target. Decreasing plasma temperature leads to the well-known sequence of density regimes, from the sheath limited case with high SOL plasma temperatures, to the high recycling regime with high density and reduced target temperatures, up to the detachment phase where the plasma temperature on the targets is less than 2eV, with strong plasma recombination. Plasma detachment occurs when significant momentum, energy and particle losses take place along the field line between the SOL upstream location and the divertor target, as one can also see from extended two-point model considerations [see Ref. 4]. Due to the tremendous challenge of heat and particle exhaust in future tokamak fusion reactors, detachment is being extensively studied in a number of tokamaks, such as JET [5], TCV [6, 7], ASDEX Upgrade [8], DIII-D [9], JT-60U [10], C-Mod [11] and many others. Although detachment has an advantage in terms of heat flux and erosion issues on target, pushing detachment too far can lead to degradation of the pedestal pressure in H-mode and lower the overall confinement [12]. Moreover, the control of the detachment front, obtained for short time discharges in current tokamaks, remains a challenge for long pulses relevant for reactor operation.

Current developments investigate more complex magnetic geometries, with multiple X-points in the divertor such as snowflake divertor [13, 14] and X-divertor [15]. These geometries are expected to bring benefits for heat and particle exhaust, such as easier access to detachment (e.g. with lower plasma density), higher heat flux dissipation capabilities and more stable control of detachment front, based on the 2-point model analyses [16-18].

In order to get a deeper insight into the plasma behavior in these complex magnetic configurations, an effective simulation tool is required to properly estimate the heat and particle fluxes on the targets and wall surfaces, and understand how divertor detachment proceeds. At present, there are several edge plasma simulation codes widely used in tokamak devices: SOLPS5.2 [19], SOLPS-ITER [20], UEDGE [21], EDGE2D [22]. In this work, we use SolEdge2D which can provide solutions for particle and energy transport in the edge plasma with complex and realistic 2D magnetic and wall geometries. This code has been coupled with the Monte Carlo code Eirene modelling the transport and the complex atomic and molecular physics of neutrals (atoms, molecules) within the plasma. Thanks to the standard explicit domain decomposition technique, it can treat complex magnetic configurations like double null divertor as well as snowflake configurations. Using the penalization technique, the complex and realistic geometries of chamber wall can be handled. These features make SolEdge2D-EIRENE an efficient tool to investigate edge plasma transport, thermal exhaust and detachment behavior in tokamak devices, as illustrated by its application to several machines including HL2M [23], WEST [24], JET [25], TCV [26] as well as in linear devices like Pilot-PSI [27].

In this paper, we study the impact of plasma geometry on the detachment process for HL-2M scenarios in L-mode plasma. In section 2, we introduce the HL-2M device. In section 3, the 2-point model is briefly recalled and the potential of alternative divertor configurations is discussed in terms of basic geometrical properties. In section 4, we present the simulation results of density ramps for a typical SF- configuration. We also explore the detachment process in SF+ and SF- configurations in section 5. From the comparison of detachment features for these three configurations (threshold, degree and detachment window), the impact of the magnetic configuration and the divertor geometry have been investigated.

2. HL-2M Tokamak and configurations

The simulations are run for the preparation of the tokamak HL-2M, currently under ~~in~~ construction at the SWIP laboratory [28]. HL-2M aims at investigating the potential benefit of advanced divertor geometries with respect to the reduction of peak heat loads onto the divertor targets, with up to 20MW of additional power available. The typical operational parameters are as follows:

TABLE I. TYPICAL OPERATIONAL PARAMETERS FOR HL-2M

Plasma current I_p (MA)	**1.2**
Toroidal field Bt (T)	**2.2**
Major radius R_0 (m)	**1.78**
Minor radius a (m):	**0.65**
Elongation κ	**1.8 - 2**
Triangularity δ	**> 0.5**
Volt-second ΔΦ (Vs)	**14**
Heating power (MW)	**20**

Flexible magnetic configurations will be provided by 16 independently powered poloidal field coils, represented in figure 1. This allows an extreme flexibility both in the core plasma shape, with a large variety of shaping parameters available, as well as in divertor configurations. For the first phase of the project, divertor surfaces will be carbon materials, and stainless steel for the remaining main chamber.

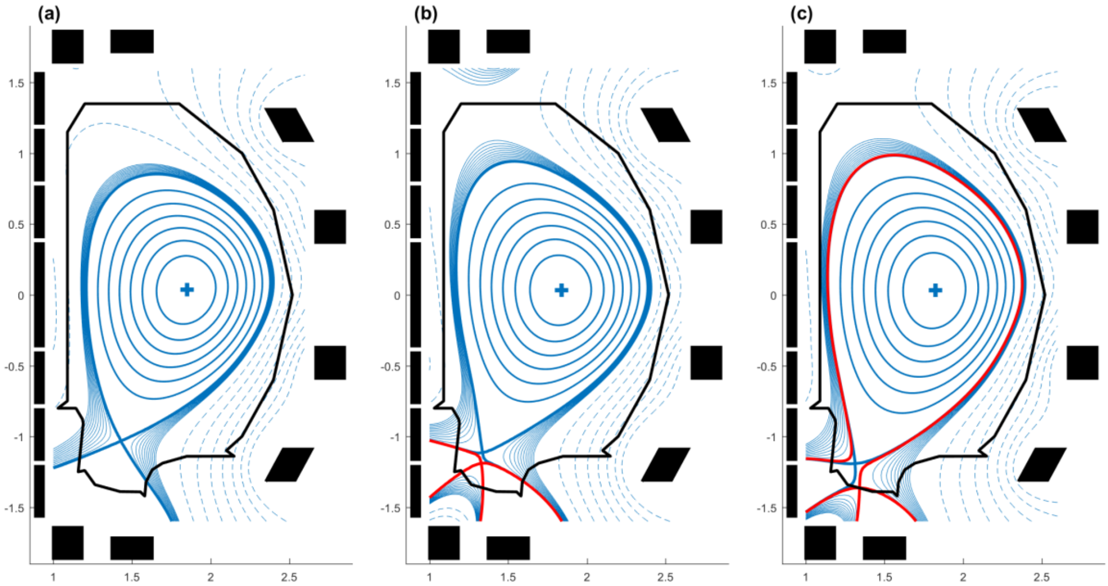

Figure 1. HL2M cross section with the 16-poloidal field coils (black boxes). (a) single null (SN), (b) snowflake plus (SF+), (c) snow flake minus configuration (SF-). The blue lines represent the cross section of the magnetic flux surfaces, while the red lines represent the flux surface corresponding to the second X-point. The black line represents the wall geometry of the vacuum vessel.

3. 2-point model estimations on the impact of divertor geometry

In this section, we investigate the impact of divertor magnetic geometries in terms of detachment behavior and heat exhaust, based on the 2-point model [4]. We focus on the outer divertor leg and the corresponding schematic geometries of the three magnetic configurations are shown in Figure 2. Based on the 2-point model, we assume that heat flux ($\mathrm{q_u}$) enters the scrape-off layer through the outboard midplane and flows along the magnetic field line to the divertor plate. In the following, the notations A_u and A_t stand for the value taken by the quantity A at respectively upstream positions (midplane) and target positions (divertor surface).

First, we assume that the total pressure is conserved along field lines:

$$n_u T_u = 2 n_t T_t \tag{1}$$

Then, the parallel heat flux along the SOL is approximated by its conductive part:

$$q_\parallel = -\kappa_0 \frac{2}{7} \nabla_\parallel T_e^{7/2} \tag{2}$$

where κ_0 is the Spitzer conductivity $\left(\kappa_0 = 3.16 \frac{e n_e v_{th,e}^2}{\nu_e T_e^{5/2}} \approx 2000\ W m^{-1} eV^{-\frac{7}{2}}\right)$, ν_e the electron collision rate, $v_{th,e}$ the thermal velocity for electrons. This expression is supposed to hold along the main fraction of SOL field lines. Simply assume the gradient to take place along the length of the SOL field lines $L_\parallel$:

$$T_u^{7/2} = T_t^{7/2} + \frac{7 q_\parallel L_\parallel}{2\kappa_0} \tag{3}$$

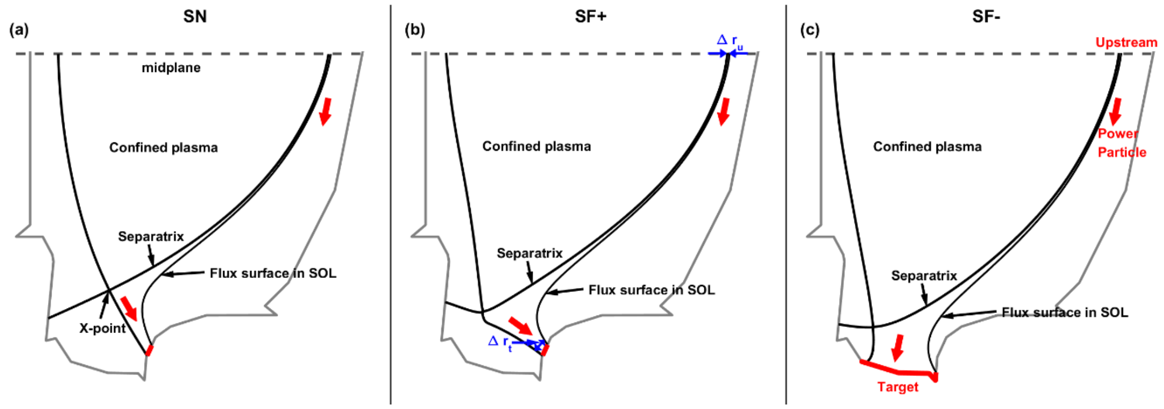

Figure 2. Schematic geometries of parallel heat/particle transport in a flux tube between the separatrix and a neighboring flux surfaces in the SOL, from the upstream location (outer midplane) to the outer target. Red arrows indicate the heat/particles fluxes.

At the target, the expression of the parallel heat flux is given by the Bohm boundary condition and reads:

$$q_\parallel = \gamma c_s n_t T_t = \frac{\gamma \sqrt{Z+\alpha}}{\sqrt{m_i}} e^{3/2} n_t T_t^{3/2} \tag{4}$$

where $\gamma \approx 5 + 2.5\alpha$ is called the sheath transmission coefficient and Z is the ion charge. Here α is such that $T_e = \alpha T_i$ and is assumed to be constant along field lines. For $T_e = T_i$, we therefore have $\gamma \approx 7.5$, which takes into account both electron and ion heat loads, including the acceleration of ions and repulsion of a fraction of the electrons in the sheath.

In high recycling regime with a cold plasma at the target (high collisionality), one has $\left(\frac{T_t}{T_u}\right)^{7/2} \ll 1$, and equation (3) is simplified into:

$$T_u^{7/2} = \frac{7q_\parallel L_\parallel}{2\kappa_0} \tag{5}$$

Then, using the pressure conservation equation (1) and the Bohm boundary condition on the heat flux, equation (4), we get:

$$n_t = \frac{n_u^3 T_u^3 C^2}{8q_\parallel^2} \propto \frac{n_u^3 L_\parallel^{6/7}}{q_\parallel^{8/7}} \tag{6}$$

$$T_t = \frac{4q_\parallel^2}{n_u^2 T_u^2 C^2} \propto \frac{q_\parallel^{10/7}}{n_u^2 L_\parallel^{4/7}} \tag{7}$$

$$\Gamma_i \propto n_t\sqrt{T_t} \propto \frac{L_\parallel^{4/7}}{q_\parallel^{3/7}} n_u^2 \tag{8}$$

$$with\ \ C = \frac{\gamma\sqrt{Z+\alpha}}{\sqrt{m_i}} e^{3/2}$$

From these simple two-point model equations, we define the detachment onset as low plasma temperature on the target, $\mathrm{T}_t \sim 5\mathrm{eV}$. With constant $q_\parallel$ we can get the relationship between $L_\parallel$ and n_u from equation (7): $n_u \propto L_\parallel^{-2/7}$. Thus, increasing parallel connection length, one expects a reduction in upstream density for detachment proportional to $L_\parallel^{-2/7}$.

Taking into account the effect of the total flux expansion $f_R = B_u/B_t \approx R_t/R_u$, the modified 2-point model [29] is given by:

$$n_t \propto \frac{n_u^3 L_\parallel^{6/7}}{q_\parallel^{8/7}} f_R^2 \left(\frac{ln f_R}{f_R - 1}\right)^{6/7} \tag{9}$$

$$T_t \propto \frac{q_\parallel^{10/7}}{n_u^2 L_\parallel^{4/7}} \frac{1}{f_R^2} \left(\frac{ln f_R}{f_R - 1}\right)^{-4/7} \tag{10}$$

This model shows that increasing f_R can shift the detachment onset towards lower upstream density and enhance the detachment control performance [18].

The power flowing down the divertor can be expressed as:

$$\frac{1}{2} P_{sep} = 2\pi R \lambda_q q_\parallel \frac{B_\theta}{B} \approx 2\pi R \lambda_q q_\parallel \frac{B_\theta}{B_\phi} \tag{11}$$

Here, B_θ can be neglected compared to B_ϕ (hence $B \simeq B_\phi$). Here, B is the total magnetic field, B_θ and B_ϕ denote the poloidal and toroidal components of the magnetic field. Taking into account geometrical effects due to the magnetic flux expansion f_x^*, and the geometry of the divertor target, the heat flux deposited on the divertor can be expressed as:

$$q_t = \frac{R_u}{R_t}\frac{sin\beta}{f_x^*}q_{\parallel} \approx tan\alpha_t \frac{B_{\phi,u}}{B_{\theta,u}}\frac{P_{sep}}{4\pi R_t \lambda_q} \quad (12)$$

with β the angle of divertor target inclination with respect to flux surfaces and f_x^* the volumetric flux expansion, defined as $f_x^* = \frac{\Delta r_t}{\Delta r_u} = \frac{B_{\theta,u}R_u}{B_{\theta,t}R_t} = \frac{B_{\theta,u}B_{\phi,t}}{B_{\theta,t}B_{\phi,u}}$. Here $\frac{\Delta r_t}{\Delta r_u}$ is the ratio between the distance of two close flux surfaces taken at the target and upstream locations respectively. α_t represents the incidence angle of the magnetic field line on the divertor plate.

From Eq. (12), there are two ways for reducing the peak heat flux perpendicular to the divertor plate. One possibility is to reduce the angle α_t by tilting the divertor plate (or by increasing the volume flux expansion f_x^*). And the second way is to bring the outer strikepoint to a larger major radius to increase the factor R_t. It should be noticed that, in reactor relevant conditions with actively cooled divertors composed of castelleted plasma facing units, there is an engineering limit on how small the incidence angle can be [30]. This necessarily limits the achievable reduction of heat flux by wall tilting and flux expansion. With the ITER monoblock technology, a minimum incidence angle of 1.5 degree is envisaged.

One possible approach to solve the heat exhaust issue is to develop robust strategies for controlling detached plasmas, increase the radiation in the divertor volume, and thus distribute P_{sep} over a much larger surface area around the strike points. From the 2-point model equation (7), an increase of the parallel connection length could be beneficial to reduce the temperature on target and ease detachment access. This can be achieved by lowering the poloidal magnetic field in the divertor, in other words increasing the volume flux expansion. It has also been proposed that poloidal flux expansion [18] and flux flaring near the target shall improve detachment stability.

4. SolEdge2D-Eirene code and plasma simulations in snowflake minus divertor configuration

The transport code SolEdge2D-EIRENE has been developed in the perspective of simulating the entire volume of edge plasma interacting with the wall in tokamaks. It is based on a standard explicit domain decomposition technique, allowing one to treat various magnetic configurations, from limiter plasma to complex double null divertor scrape-off layers, or even snowflake configurations. The computational grid has been divided first into several subdomains that are topologically different (core, SOL, Private Flux Region - PFR, and so on). Then each subdomain is further divided into several zones solved in parallel to reduce the computation wall clock time, each zone having a similar number of grid points. The specificity of the plasma solver SolEdge2D is to use an immersed boundary condition technique, termed here ‘penalization’, in order to enable simulations of the plasma up to the first wall in a flexible manner [31, 32]. As an illustration, the meshes of SN, SF+ and SF- configurations for the HL-2M device are plotted in figure 3, and are also used for simulations analyzed later. As shown in figure 3, the SolEdge2D code relies on flux surfaces aligned meshes and these meshes are not intrinsically suitable to describe the first wall geometry, which is not aligned on the flux surfaces. Thanks to the penalization technique, we are able to overcome this issue and extend the mesh grid up to the wall, verifying Bohm boundary conditions at the plasma-wall interface. Because of the parallelization over zones, splitting the domain into a large number of zones can accelerate the speed of convergence.

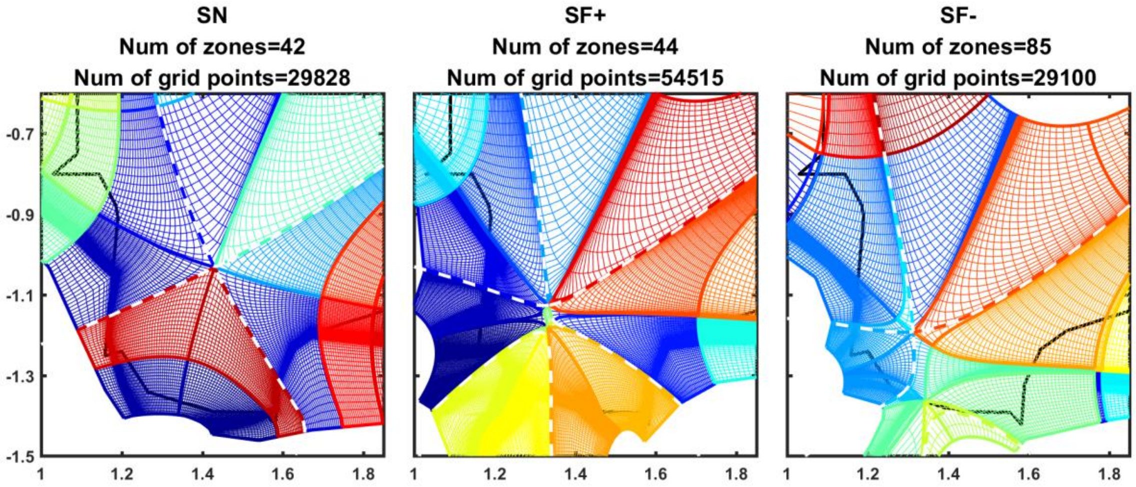

Figure 3. Grid of HL-2M SN, SF+ and SF- configurations used for SolEdge2D-EIRENE code. The different color lines represent the grids, the black solid line under the grids represents the wall of vacuum chamber, and the white dash line represents the plasma separatrix.

In this contribution, we consider only pure Deuterium plasma, so the SolEdge2D version we use simulates plasmas made of two species: singly charged ions and electrons. For each species, one solves equations for density n, parallel velocity u and temperature T. The quasi-neutrality and ambipolarity assumptions give $n_e = n_i$ and $u_e = u_i$. The transport of mass, parallel momentum and energy equations are solved using a finite volume numerical scheme. The inertia and viscosity terms of the electrons are neglected so that the parallel electric field is given by the relation $\mathrm{enE}_{\parallel} = -0.71\mathrm{n}\nabla_{\parallel}T_e - \nabla_{\parallel}(\mathrm{nT_e}) - \mathrm{R_{ei}}$ where the first rhs term is the thermal force, the second is the pressure gradient and $\mathrm{R_{ei}}$ is the parallel electron–ion friction force. In this paper, there is no impurity, no currents $(u_e = u_i$, so that $\mathrm{R_{ei}} = 0)$. The cross-field (perpendicular) turbulent transport is modelled by an ad hoc diffusion–convection model. In that sense, the perpendicular particle flux is expressed as $\mathrm{n}\vec{\mathrm{u}}_{\perp} = -\mathrm{D}\vec{\nabla}_{\perp}\mathrm{n} + \mathrm{n}\vec{\mathrm{v}}_{\mathrm{pinch}}$. The perpendicular anomalous diffusivities D, ν and χ and pinch velocity $\vec{\mathrm{v}}_{\mathrm{pinch}}$ must be determined either from experimental data or numerical simulations of turbulence. The particle (S^{n}), momentum $(S^{\mathrm{nu}_{\parallel}})$ and energy (S^{E}) source terms due to interactions with neutrals (atoms, molecules) are computed with EIRENE.

In the parallel direction, Bohm boundary conditions are imposed at the magnetic pre-sheath entrance (MPSE), that is $|u_{BC}| \geq C_s = \sqrt{\frac{T_e+T_i}{m_i}}$. The parallel heat flux is set to $q_{\parallel BC} = (\gamma nTu_{\parallel})_{BC}$ with default values $\gamma_i = 2.5$ and $\gamma_e = 4.5$ for the sheath heat transmission coefficients.

We consider the detachment in SF- configuration using density ramps and with a simulation set up related to parameters listed in table 1. Some basic characteristics of this density ramp simulation are illustrated in figure 4 along with the magnetic geometry. In figure 4(a), the SF-configuration for HL-2M has been shown, the blue arrow 1#, 2# mark the strike points for separatrix, and the red arrow 3#, 4# mark the strike points for the flux surface corresponding to the second X-point. The black solid lines represent the chamber wall, and the green lines on the wall represent the active pumping, $v_{pumping} = 50\,m^3/s$. The recycling coefficients of the walls is 0.99. The drifts, neutral-neutral collisions and D2 molecules are not taken into account.

In the simulations, we ramp the electron density on the core–edge interface from $1 \times 10^{19} m^{-3}$ up to $7 \times 10^{19} m^{-3}$, thus increasing the separatrix density (n_{sep}) from $0.4 \times 10^{19} m^{-3}$ to $2.4 \times 10^{19} m^{-3}$, see figure 4(b). The power injected into the SOL region is fixed at 1.5 MW, and the radiated power increases throughout the density ramp, as shown in figure 4(d).

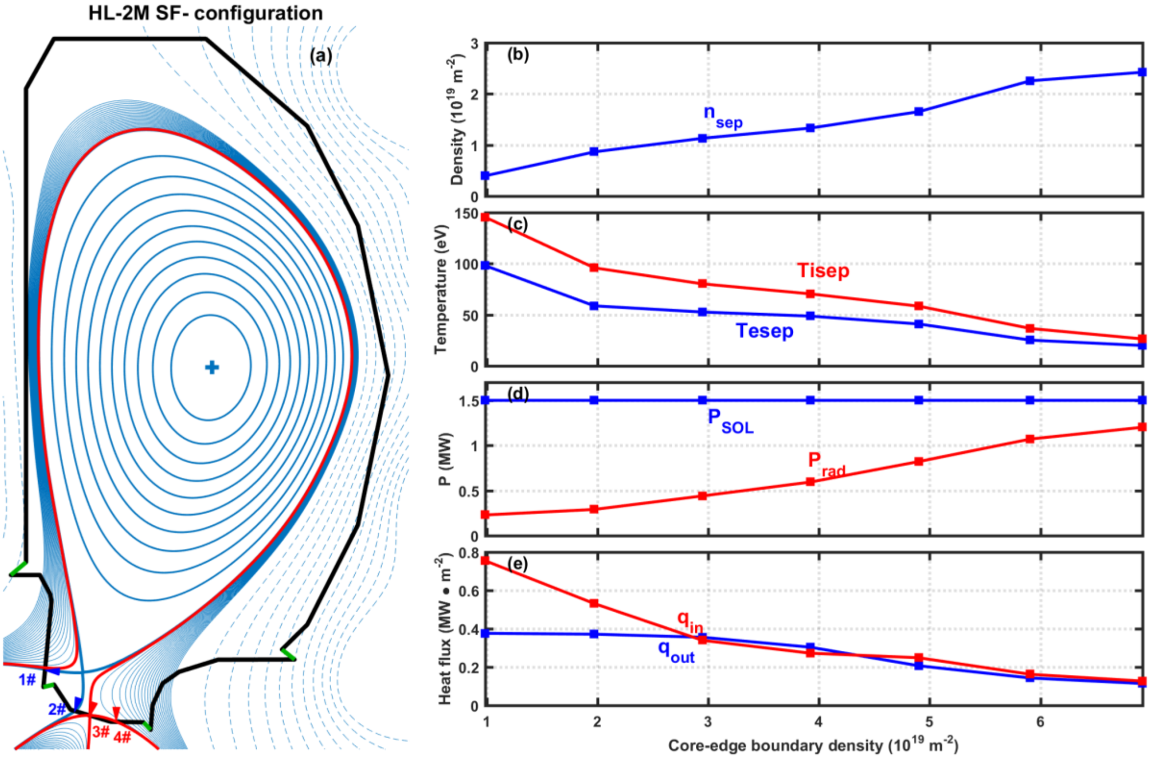

Figure 4. (a) SF- magnetic equilibrium. (b) separatrix electron density on midplane, also called upstream density. (c) upstream electron temperature (blue line) and ion temperature (red line). (d) Power injected into the SOL region (blue) and radiative power computed during the simulation (red). (e) peak value of heat flux outer target (blue line) and inner target (red line).

Parameter	D	ν	$\chi_e \chi_i$	P_{in}	n_{cb}
Value	$1\,m^2s^{-1}$	$0.6m^2s^{-1}$	$2m^2s^{-1}$	1.5MW	$1 \times 10^{19} - 7 \times 10^{19} m^{-3}$

Table 2. Input parameters for the SolEdge2D–EIRENE simulations. D is the cross-field mass diffusivity perpendicular to the flux surface, $\boldsymbol{\nu}$ the momentum diffusivity, $\boldsymbol{\chi_e}, \boldsymbol{\chi_i}$ the heat flux diffusivity for electrons and ions. P_{in} is the power flux entering the simulation domain at the core–edge interface, equally shared by ions and electrons. n_{cb} is the density at the core–edge interface.

As an illustration, figure 5 shows 2D contour plots of density, parallel Mach number, electron and ion temperature for the HL-2M snowflake minus configuration and the simulation parameters are listed in table 2. We put the $\mathrm{v_{pinch}} = 0$ in these simulations. Simulation setup is always time-dependent due to the explicit time marching numerical algorithm implemented in SolEdge2D, but we analyze only the final steady state for each density value.

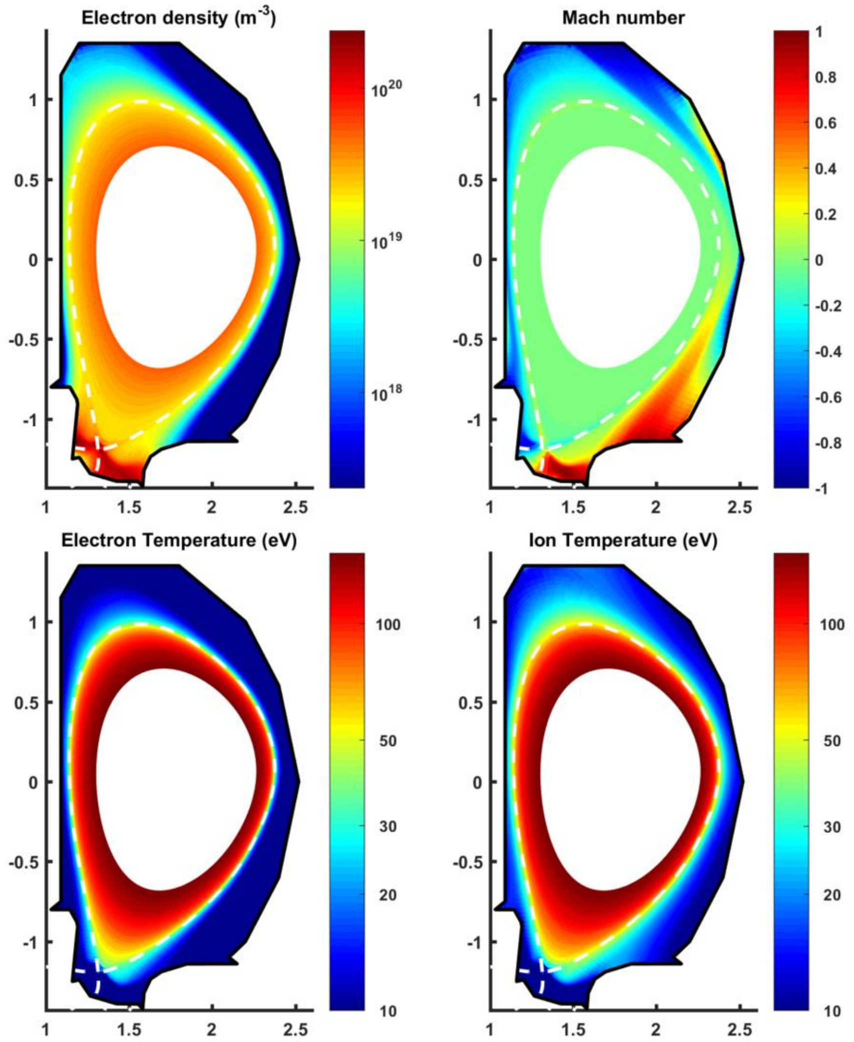

Figure 5. Example of SolEdge2D–EIRENE 2D outputs for the SF- plasma: density, parallel Mach number, electron and ion temperature profiles for a pure deuterium plasma with P_{in} = 1.5 MW and $n_{sep} = 1.65 \times 10^{19}\ m^{-3}$. The transport parameters are shown in table 2.

In figure 6, we present some key features of the detachment process on the outer target for the density ramp simulation shown in figure 4. In figure 6(a), the black line represents the ion particle flux Γ_i which is expected to be proportional to n_u^2 according to the 2-point model in high-recycling regime, equation (8). In figure 6(a), the orange line shows the peak value of the ion flux on the outer target as a function of the separatrix density. Initially, the ion flux increases approximately linearly with the separatrix density, then clearly rolls over at $n_{sep} = 1.65 \times 10^{19} m^{-3}$, characterizing the onset of detachment. A degree of detachment (DoD) can be defined as the ratio of the target ion flux expected from the 2-point model and the simulation result [5, 6], the DoD being $\gg 1$ for deep detachment. The DoD, orange line in figure 6(b), reaches values up to 15. It should be noticed that the value of DoD is not absolute, it depends on the separatrix density, for which we force DoD=1, and in this case we use the lowest density.

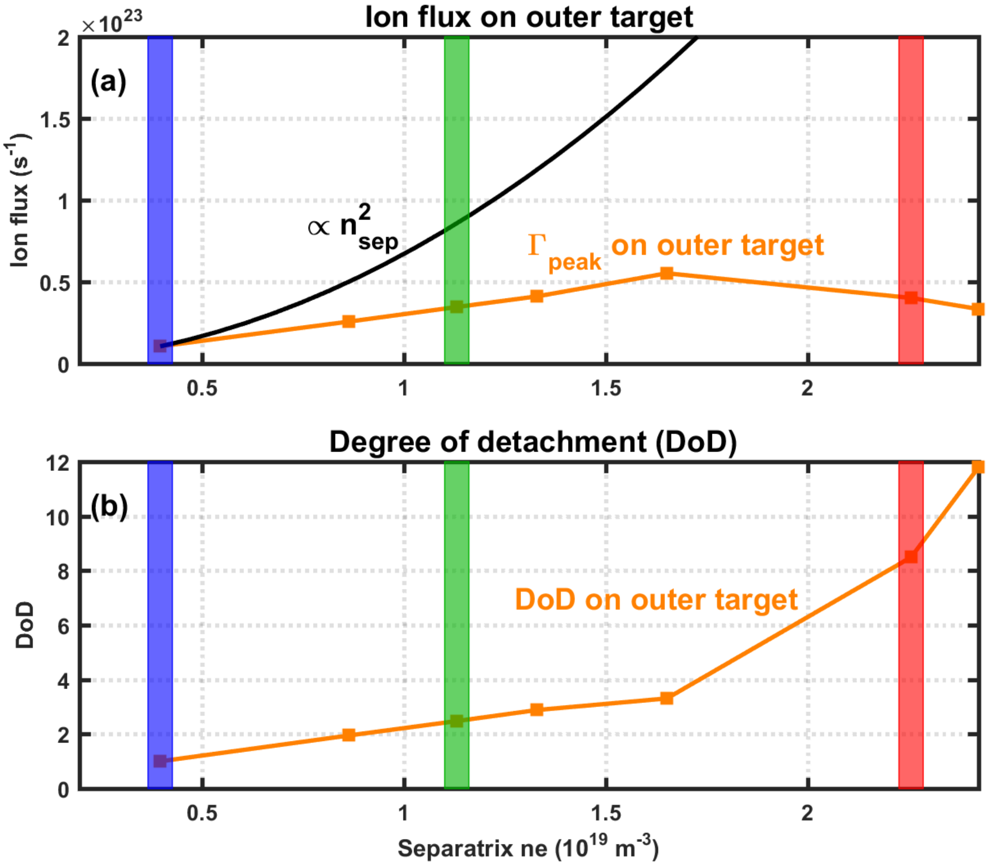

Figure 6. (a) Peak value of ion particle flux on the outer target (orange line) and expected ion particle flux based on 2-point model estimations (black line), expected to be proportional to $\langle n_u \rangle^2$. (b) Degree of detachment (DOD) on the outer target (orange line). The shaded region represents the three different plasmas, with separatrix densities $n_{sep} = 0.40 \times 10^{19} m^{-3}$ (blue), $n_{sep} = 1.13 \times 10^{19} m^{-3}$ (green), $n_{sep} = 2.26 \times 10^{19} m^{-3}$ (red). Profiles for these plasmas are shown in figure 7, using the same color code.

In figure 7, the density, electron temperature and total pressure profiles at the outer midplane and the divertor plate have been compared for different stages in the detachment process. Here, subscripts u and t denote upstream and target quantities and we use the normalized poloidal flux, $\psi_x = (\psi - \psi_m)/(\psi_b - \psi_m)$ as radial coordinate, where ψ_m is the poloidal flux value at the magnetic axis, and ψ_b ~~is~~ its value at the separatrix. The three columns of profiles correspond to the three different separatrix densities marked by shaded regions in figure 6, the same color code being used. At the lowest density (right), the electron temperature and pressure match~~es~~ across the SOL between midplane and divertor target, indicative of the sheath limited regime, as shown in figure 7(b, c). Here the divertor electron pressure is normalized by a factor of 2 to account for the dynamic pressure of the sonic flow into the sheath in front of the target. At intermediate density, figure 7(e, f), a clear temperature gradient along the magnetic field already exists, Te on target is reduced to <20 eV. This is the high recycling regime~~s~~. In the region near the strike point, Te is below 10 eV, figure 7(e), the pressure on target drops below that observed on the midplane, which indicates a local detachment at the strike point. This drop occurs in the near SOL with pressure balance still maintained in the far SOL. Finally, for the highest density case, Te on the target drops below 5 eV and a clear pressure gradient along the field is established on the entire target, figure 7(h, i).

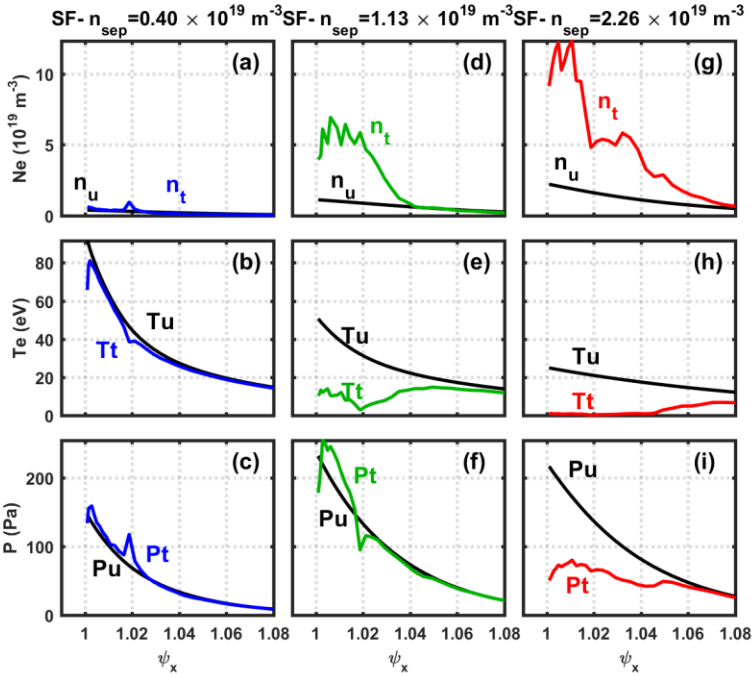

Figure 7. Comparison of density, temperature, and pressure profiles at the upstream (midplane) and the outer target versus increasing densities for SF- configuration. The left column corresponds to the lowest separatrix density, as well as the blue shaded region in figure 6. The middle and right column correspond to intermediate and highest densities, also to the same color shaded region in figure 6.

The evolution of radiation profiles during the detachment process driven by separatrix density ramps are shown in figure 8. Focusing on the radiation along the outer leg, it is clear that, initially, the radiation region is concentrated near the strike point (figure 8(a)). Later in time, as the plasma density increases, and leg cools down (figure 8(b) and (c)) the front of the radiation region moves upstream towards the X-point. In the following, we will use the front of the cold, radiative region as the location of the detachment region. We determine this location as the position where the radiation power along the outer leg has dropped to half of its peak value. Then we evaluate the connection length of front edge along the outer leg between the strike point and X-point as a function of separatrix density. The result of this analysis is presented in figure 8(d).

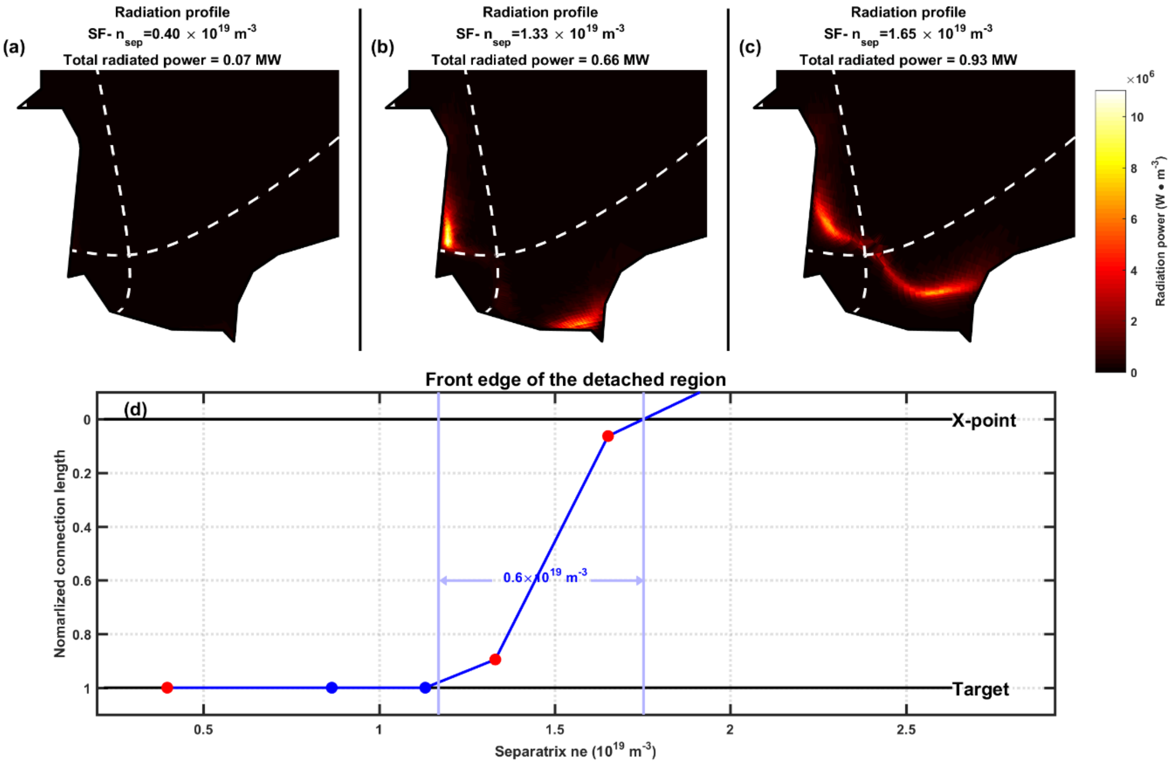

Figure 8. (a)–(c) Radiation profiles in the divertor volume for different time periods during the density ramp simulations in figure 4. (d) Position of the radiation front along the outer leg as a function of separatrix density (blue dots). The red dots represent the three different density cases as shown above (a-c).

From the figure 8(d), the radiation starts to detach from the target at a separatrix density $n_{sep} = 1.13 \times 10^{19} m^{-3}$, and reaches the X-point at $n_{sep} = 1.75 \times 10^{19} m^{-3}$. The density window between the start of the radiation front movement and when it arrives at the X-point is $\Delta n_{sep} \sim 0.6 \times 10^{19} m^{-3}$.

The simulation results presented in this section show key characteristics of detachment, such as reduction of particle and heat fluxes reaching the target, a cooling of the plasma in the divertor leg, and the increase of parallel pressure gradients. In the following, when we compare the detachment behavior in different geometries, we mainly focus on the integrated and local drop of ion particle flux, energy dissipation, and pressure loss along the outer divertor leg from upstream (midplane) to target. The amplitude of the roll-over in ion particle flux and pressure are used as an indication of the level of detachment, and the upstream density range between the start of the radiation front movement and when it arrives at the X-point, is called the detachment window.

5. The impact of alternative diverter configurations

We now explore the effect of alternative divertor configurations. The detachment process in SN, SF+ and SF- configurations have been simulated with the same parameters as for the SF- cases, listed in table 1. In figure 9 (d) - (f), the radial profile of poloidal flux expansion f_x, connection lengh $L_{\parallel}$ and incidence angle α_t along the outer divertor plate are plotted against the normalized magnetic flux ψ_x. The corresponding magnetic equilibriums are shown in figure 9 (a)-(c). For the SF+ configuration, the additional X-point in the private flux region strongly increases ~~the~~ $L_\parallel$ near the strike point, as shown in figure 9(e). At the flux surface closest to the separatrix, $\Delta\mathrm{r}\sim 0.1\mathrm{mm}$ on midplane, the parallel connection length is $L_\parallel \approx 120\ m$ for SF+ and $L_\parallel \approx 20\ m$ for SN. But the other geometry parameters, f_x and α_t, have not been affected and the position of strike points is also similar. In the SF- configuration, the second X-point in the SOL region obviously increases the flux expansion f_x, by a factor from 2 to 10, for the whole divertor target, figure 9(d). The incidence angle on the target has also been reduced from $\alpha_t \approx 4°$ to $\alpha_t \approx 1°$, due to short distance between the additional X-point and target, as shown in figure 9(f).

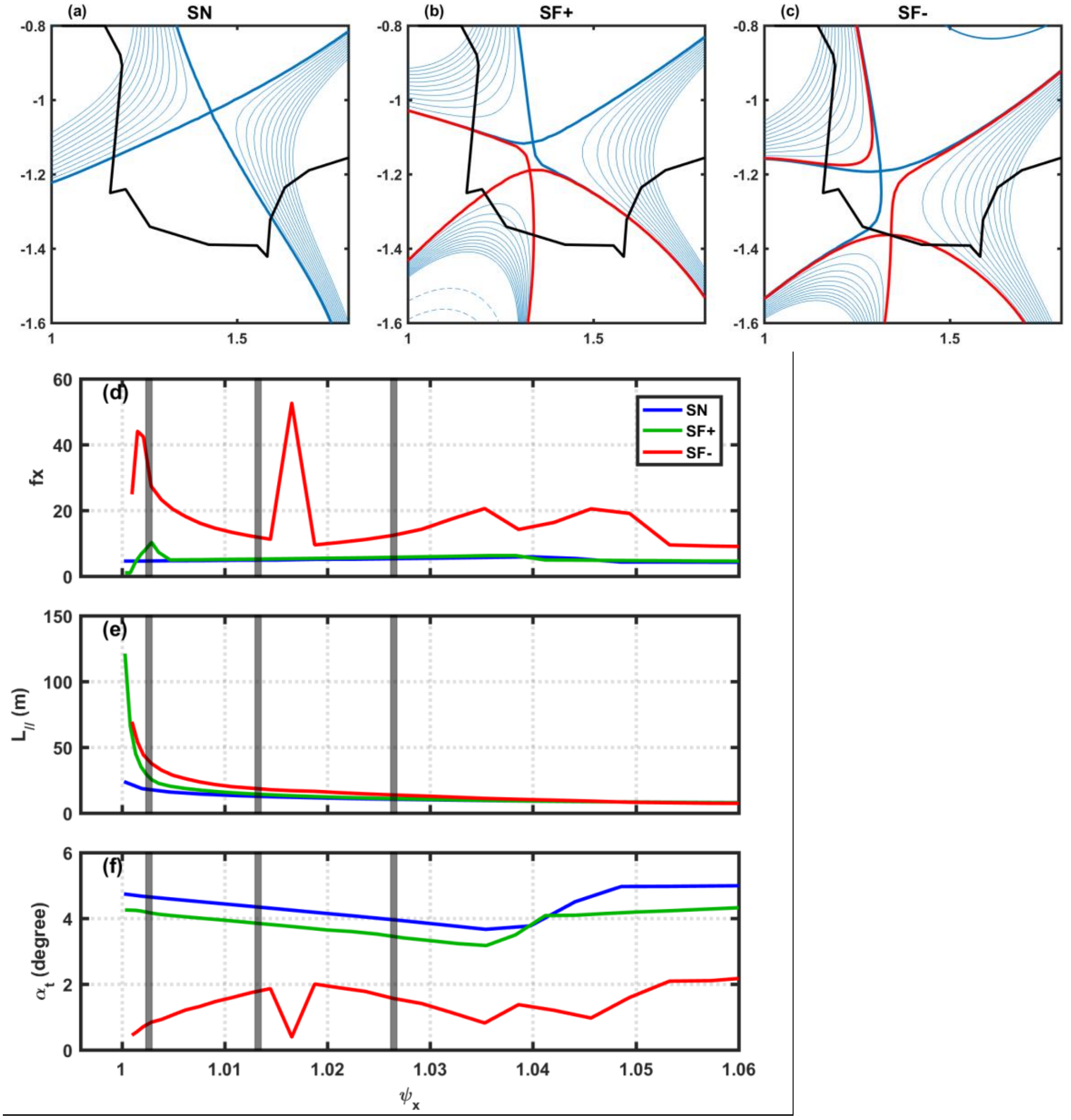

Figure 9. (a)-(c) show the divertor region of HL-2M SN, SF+, SF- configurations. For the snowflake minus plasma, the second X-point is near the wall. Panels (d)-(f) show radial profiles of poloidal flux expansion, connection length and magnetic field line incidence angles at the target of outer divertor leg. The colors correspond to the equilibria in (a)-(c). The vertical black lines represent the values of ψ_x corresponding to distances of 1mm 5mm and 10mm to the ~~from~~ separatrix at the midplane.

5.1 Impact on detachment threshold

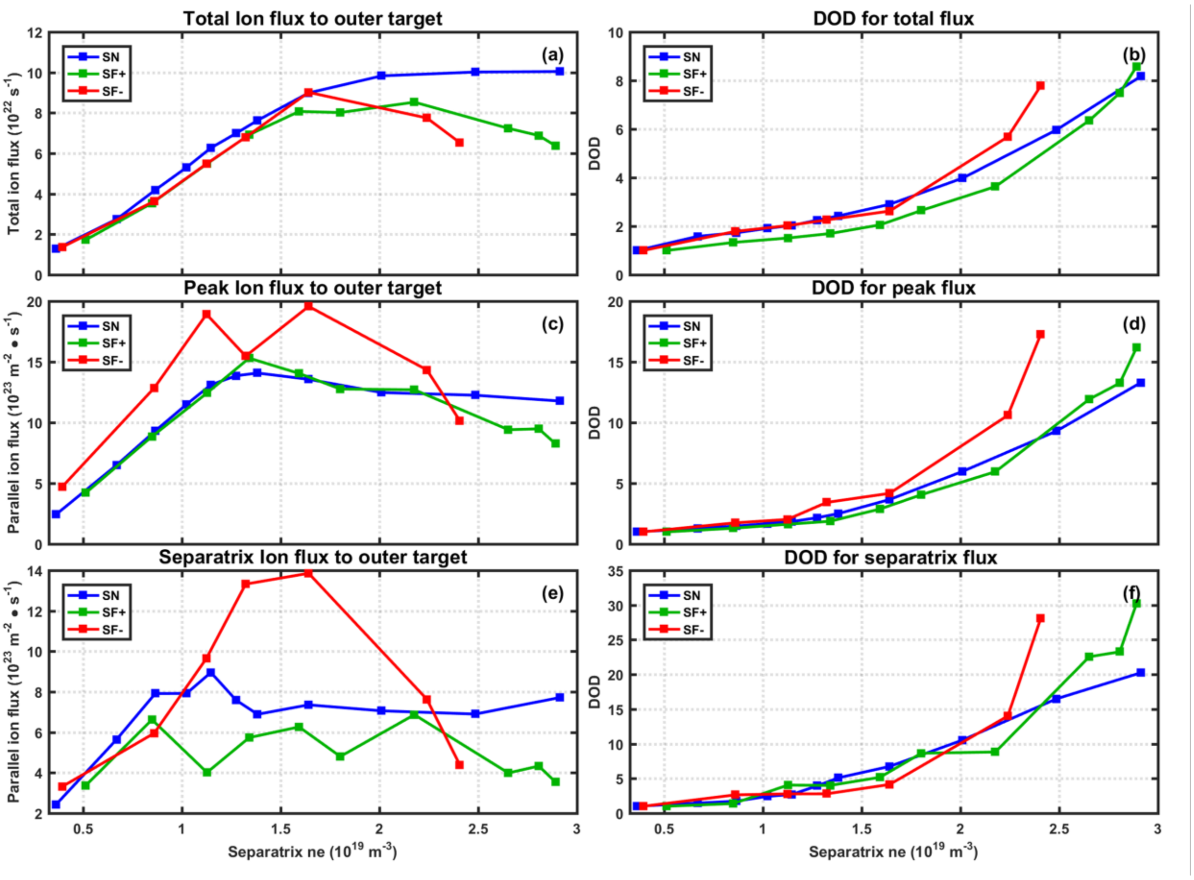

Figure 10. Ion particle flux to the outer target and the degree of detachment from the SolEdge2D-EIRENE density scan for pure hydrogen plasmas with 1.5 MW input power. On the top panel (a), the dependence of the total ion particle flux ($\int nv_i \cdot sin\alpha_t \cdot ds$) is shown as a function of midplane separatrix density for the outer target in SN, SF+ and SF- configurations, here v_i represents parallel velocity for ion. (b), the DOD for total ion flux on the outer target. On the middle vertically (c, d), the same dependence is plotted for the peak ion flux and for the DOD defined for the peak value of ion flux. The bottom panels (e, f) show the dependence of the ion particle flux at the strike point and the corresponding DOD for separatrix ion flux.

In figure 10, we plot the total ion particle flux to the outer target, its peak value and the ion flux at the outer strike point as a function of the separatrix density for different configurations. In figure 10(a), at low density, during attached plasma $(\mathrm{n_{sep}} < 1.5 \times 10^{19}\ \mathrm{m^{-3}})$, the total fluxes for the three different configurations have similar trends. As the density is increased, a roll-over is observed. The SF- configurations has a lower threshold of detachment characterized by roll-over of the total ion flux, since the SF- plasma detachment onset is observed at an upstream density of $n_e{\sim}1.6 \times 10^{19}\, m^{-3}$, while for SF+ the latter is $n_e{\sim}2.2 \times 10^{19}\, m^{-3}$ and for SN $n_e{\sim}2.5 \times 10^{19}\, m^{-3}$. The stronger drop in total flux indicates a deeper detachment is achieved for SF- at a given separatrix density. To be more quantitative, we evaluate the degree of detachment for the different configurations presented on figure 6. For detached conditions with a separatrix density of $n_e{\sim}2.4 \times 10^{19}\, m^{-3}$, the integral DOD is 5.8 for the SN configuration, 5 for the SF+ configuration and 8 for the SF- configuration, figure 10 (b).

Considering the effect of divertor closure, it appears that the SN and SF+ configurations raise the outer strike point to bring the divertor plasma above the baffle structure as illustrated in figure 1 (a, b) and thus makes these divertor configurations more open compared to the SF- one, figure 1 (c). So, the most closed divertor (SF-) has produced the highest ne and lowest Te near the strike point, compared to more open divertor configurations at the same line-averaged density (see figure 13(b, c, d)). These observations are consistent with experiment results on C-Mod [33], ASDEX-Upgrade [34] and JT-60U [35], where L-mode discharges in more open divertors required ~15% higher core density than in more closed configuration to achieve detachment of the outboard divertor.

Then we consider the parallel ion particle flux on the strike point and the peak value of the ion flux, shown in figure 10(c, e), and define the local particle detachment onset in terms of parallel ion flux roll-over on the strike point and peak ion flux, while further out into the SOL the plasma remains attached. The SN and SF+ configurations achieve local particle detachment onset at a lower upstream density, compared to the SF- configuration. The local detachment occurs at $\mathrm{n_e}{\sim}1.3 \times 10^{19}\ \mathrm{m}^{-3}$ for SF+ and SN, $\mathrm{n_e}{\sim}1.6 \times 10^{19}\ \mathrm{m}^{-3}$ for SF-. The reason might be the positioning of the outer strike point on the vertical plate for SN & SF+, while the latter is on the horizontal plate for SF-. The degree of local detachment for SN and SF+ configurations are similar, while for SF- it is substantial higher.

The local detachment simulation results from the three configurations are consistent with the accepted idea of inclining the divertor target with respect to the magnetic flux line in order to reflect recycling neutrals towards the separatrix. The higher neutral pressure near the strike point leads to higher n_e, lower T_e and promotes detachment on strike point but inhibits detachment further out in the SOL with lower neutral pressure in that region. This concept is also consistent with experiments in C-Mod and JET [33], ASDEX-Upgrade [34] and JT-60U [35].

To support this statement, in figure 11, the divertor neutral pressure and density profiles for the three different configurations are plotted. These pressure profiles are obtained for a separatrix density of $\mathrm{n_e}{\sim}1.6 \times 10^{19}\ \mathrm{m}^{-3}$, that is, well after the onset of detachment. For SN and SF+ configurations, figure 11(a, b), the region of substantial neutral pressure is close to the strike point on the outer target. But for the SF- configuration, this region is far away from the strike point, even from the strike point corresponding to the second X-point. And the peak values of the neutral pressure and density for SF- are also lower than those observed in the SN and SF+ plasmas. To have a more quantitative analysis of the neutral pressure, its peak value and the neutral pressure at the outer target are plotted in figure 12 as a function of separatrix density for the three different configurations. It is evident that the neutral pressure in SN and SF+ plasma are substantially higher than in SF- plasma, for both peak (figure 12(a)) and separatrix value (figure 12(b)).

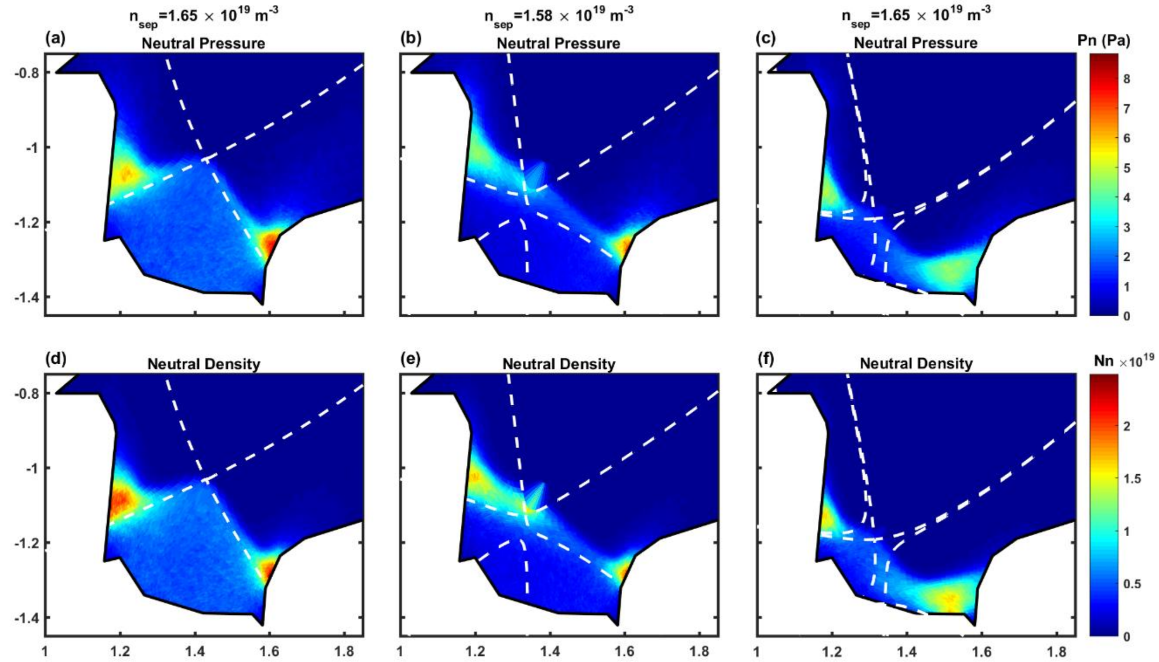

Figure 11. Neutral pressure profiles in the divertor for SN, SF+ and SF- configurations with the same input power and similar separatrix density. The white dashed lines represent the flux surface corresponding to the primary and the secondary X-points.

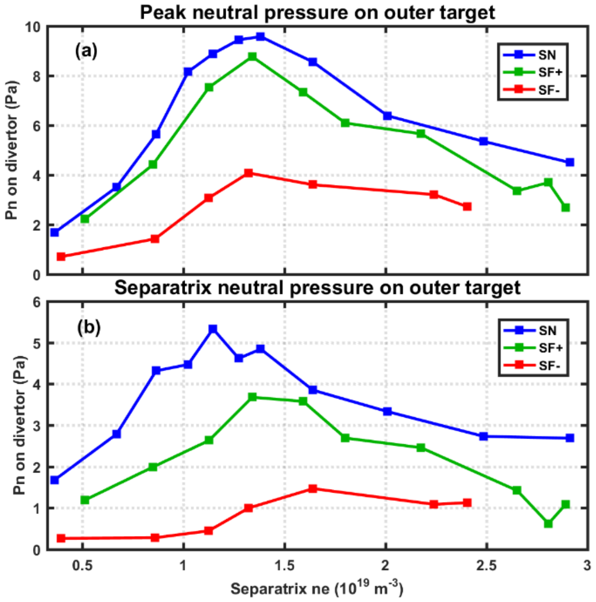

Figure 12 Neutral pressure on the outer target as a function of separatrix density for SN, SF+ and SF- configurations. The blue lines represent SN configuration, green lines represent SF+ and red lines represent SF- configuration. The peak value of neutral pressure on the outer target is shown on the top panel, and the neutral pressure on separatrix is plotted on the bottom panel.

From the 2-point model, equation (6), T_{et} is expected to scale as $\propto L_{\parallel}^{-4/7}$, so that we would expect a reduction in upstream density for detachment with in increasing $L_{\parallel}$, through the terms of $L_{\parallel}^{-2/7}$. As there is a 5-fold increase in $L_{\parallel}$ between SN and SF+ configurations in figure 9 (e), a reduction of n_u by a factor of $(5)^{-2/7} \approx 0.63$ could compensate the $L_{\parallel}$ increase according to equation (6). However, comparing the simulation results from SN and SF+ configurations in figure 10, there is not significant impact of $L_{\parallel}$ on the detachment threshold.

Considering the effect of the total expansion f_R, the modified 2-point model has a analytic scaling for T_t and f_R: $T_t \propto f_R^{-2}[lnf_R/(f_R - 1)]^{-4/7} \approx f_R^{-2}$. It is apparently that the plasma detachment onset at a lower n_u with an increasing f_R by a factor of $f_R^{-1} \approx R_u/R_t$. Comparison between SN and SF- configurations, $f_{R,SN} \approx 0.7$ $f_{R,SF-} \approx 0.65$, $L_{\parallel,SN} \approx 24$, $L_{\parallel,SF-} \approx 70$, the modified 2-point model predicts a reduction of n_u for SF- plasma detachment onset by a factor of $(70/24)^{-2/7}(0.65/0.7)^{-1} \approx 0.8$. As shown in figure 10 (a), the integral particle flux on outer target roll-over at $n_e \sim 1.6 \times 10^{19}\, m^{-3}$ for SF- and tend to be flat at $n_e \sim 2 \times 10^{19}\, m^{-3}$ for SN. However, the partial detachment onset at $n_e \sim 1.6 \times 10^{19}\, m^{-3}$ for SF- and $n_e \sim 1.3 \times 10^{19}\, m^{-3}$ for SN. Given this, the modified 2-point model predicts that the n_u for detachment onset impacted by geometry parameters as $\propto L_{\parallel}^{-2/7} f_R^{-1}$, which in good agreement with the simulation results for the integral detachment. But from the roll-over of local particle flux, the threshold of partial detachment doesn't show the effect from geometry parameter of configuration based on this modified 2-point model.

5.2 Impact on heat flux at the outer target

In order to gain some insight as to why the expected benefits of increasing $L_{\parallel}$ are not observed in these simulations, the distribution of the heat flux and other plasma parameters profiles on outer target for SN, SF+, SF- configurations are plotted on figure 13, with the similar separatrix density, and same input power. The SF- plasma has two strike points, the distance between the two strike points is $\Delta s_t \sim 170mm$, and the distance between the two flux suraface, correspond to the two strike points, on midplane is $\Delta s_t \sim 1mm$.

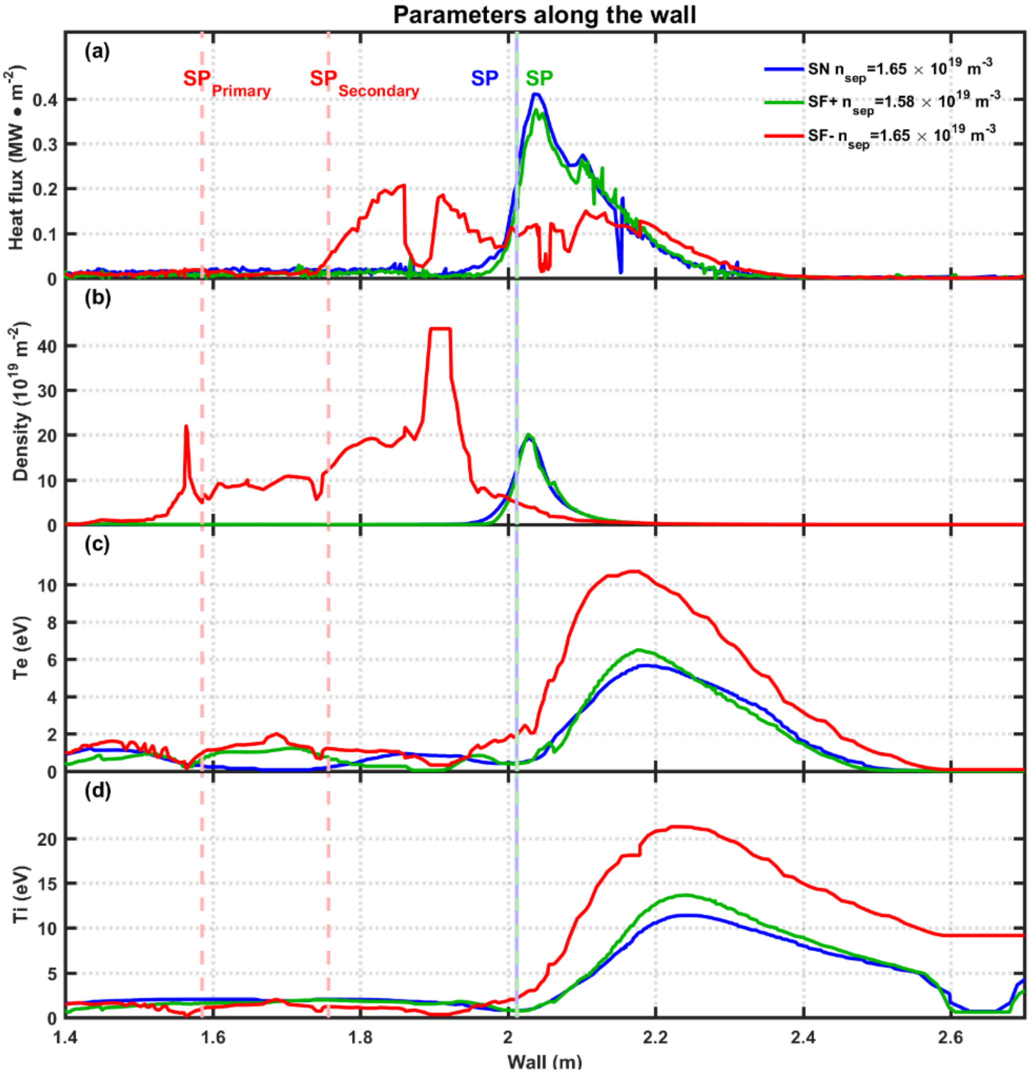

Figure 13. Heat flux, density, electron and ion temperature profile along the wall. The vertical, dash lines indicate the separatrix, corresponding to the parameter profiles with same color.

As shown in figure 13, with the small difference in separatrix density Δn_{sep}~4%, the SF+ configuration exhibited a similar parameter profiles at the outer target as the SN, even though there is a secondary X point in private region and the connection length between midplane and target $L_{\parallel}$ is much higher for SF+ as shown in figure 9 (e). As expected from 2-point model, equation (6,7), the n_t scales $\propto L_{\parallel}^{6/7}$ and the T_t scales as $\propto L_{\parallel}^{-4/7}$. However, the expected reduction of T_t and increase in n_t for SF+ plasma is absent, figure 13(b,c,d).

For SF- configuration, the peak value of heat flux obviously less than others and the region of heat load is broader. This may benefit from the density far above other configurations and the position of temperature peak far away from the strike point.

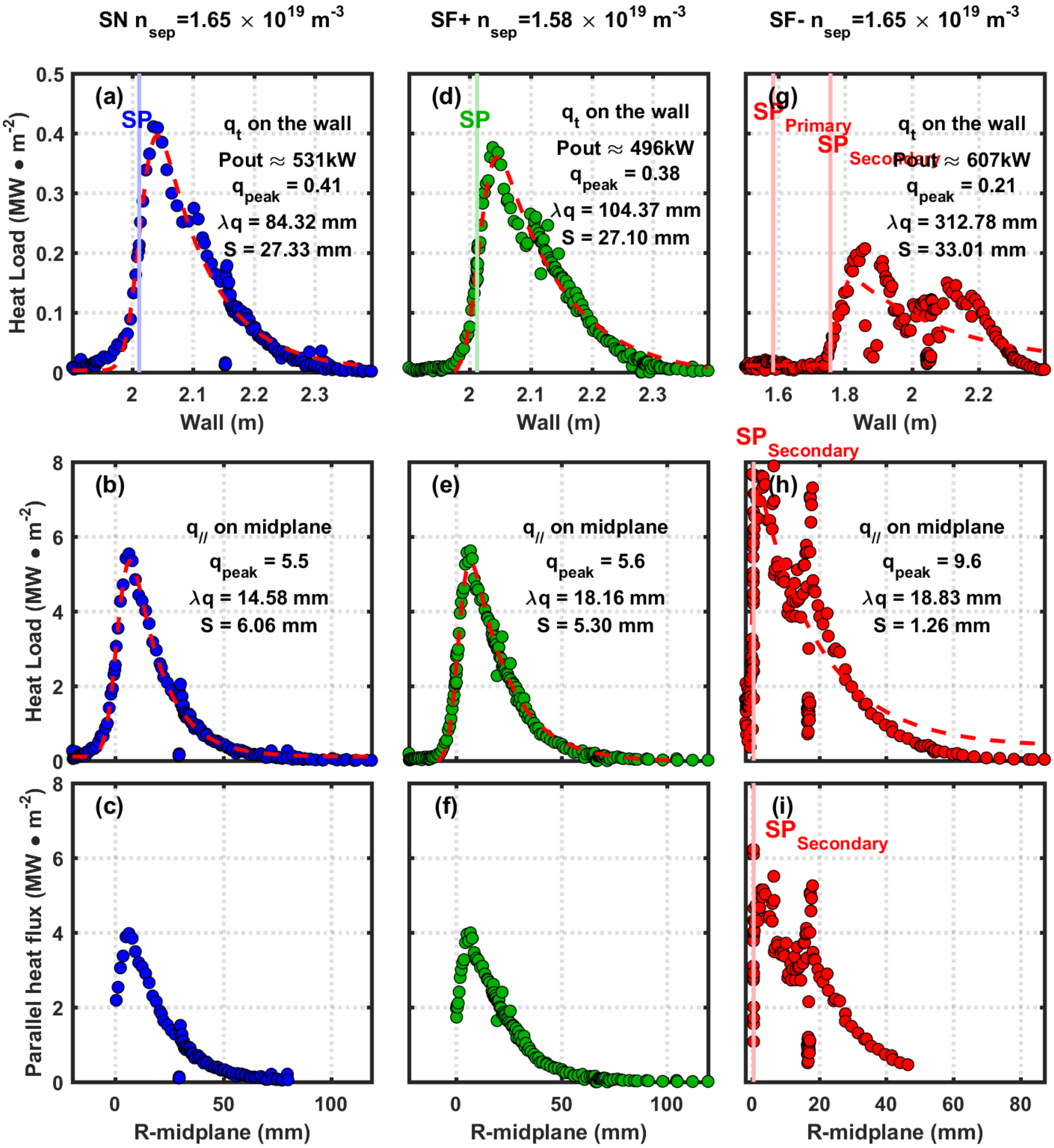

Figure 14. Top panel: Profiles of outer target perpendicular heat flux q_t for SN, SF+ and SF- configurations. Central panel: target parallel heat flux corrected by incidence angle $q_\parallel = q_t/sin\alpha_t$ and mapped to midplane for the three configurations. Bottom panel: target parallel heat flux corrected by incidence angle and total flux expansion $q_\parallel = q_t/sin\alpha_t * fx$.
The different color dots represent the simulation results for different configurations obtained with input power P_{in}=1.5MW. q_{peak} is the peak value of the profile. The parameters λ_q and S represent the width and the spreading of profiles. The dash red line is a fit of exponential spread by Gaussian [36], $f = \frac{f_0}{2} e^{\left[(S/2\lambda_q)^2-(x-x_0)/\lambda_q\right]} \times err + backgroud$. Here, f_0 is amplitude of the exponential, x_0 is center of the function, err is the complementary error function.

To have a more quantitative analysis of the effect of configurations to heat flux, the heat flux profiles on outer divertor plate q_t and the parallel heat flux profiles $q_{\parallel} = q_t / sin\alpha_t$ are shown in figure 14. Here, q_t is the total heat flux transported by plasma incidence the wall, includes the thermal of electron, ion, neutral and the recombination power of ion, without considering the radiation contribution. The $q_{\parallel}$ has been mapped to the midplane, and the radial coordinate for the below row of figure 14 is upstream radial distance to separatrix. Benefitting from the highest flux expansion f_x and lowest incidence angle, as shown in figure 9(d, f), the peak value of q_t reduces by a factor of 2, with the SF- configuration, compared to the SN and SF+ plasma. As expected in section 3, the incidence angle and flux expansion has contributed to reducing the heat load peak.

It is apparent that the q_t and $q_{\parallel}$ profiles for SN and SF+ configurations are similar, $\Delta_{peak} \approx 7\%$ $\Delta_{\lambda q} \approx 20\%$ for q_t and $\Delta_{peak} \approx 2\%$ $\Delta_{\lambda q} \approx 17\%$ for $q_{\parallel}$. The small difference on parallel heat flux between SN and SF+ plasma, combined the similar plasma parameters on the wall as shown in figure 13, indicates that the geometry parameter $L_{\parallel}$ has no impact to the plasma parameters (T_e, n_e) on the wall, to heat flux and even the detachment threshold. The reason may be that comparison to width of $q_{\parallel}$ at midplane, ~20mm as shown in figure 14(b, d), the large difference for $L_{\parallel}$ only exist in a narrow region, $< 1\mathrm{mm}$ as shown in figure 9(e).

5.3 Impact on pressure loss

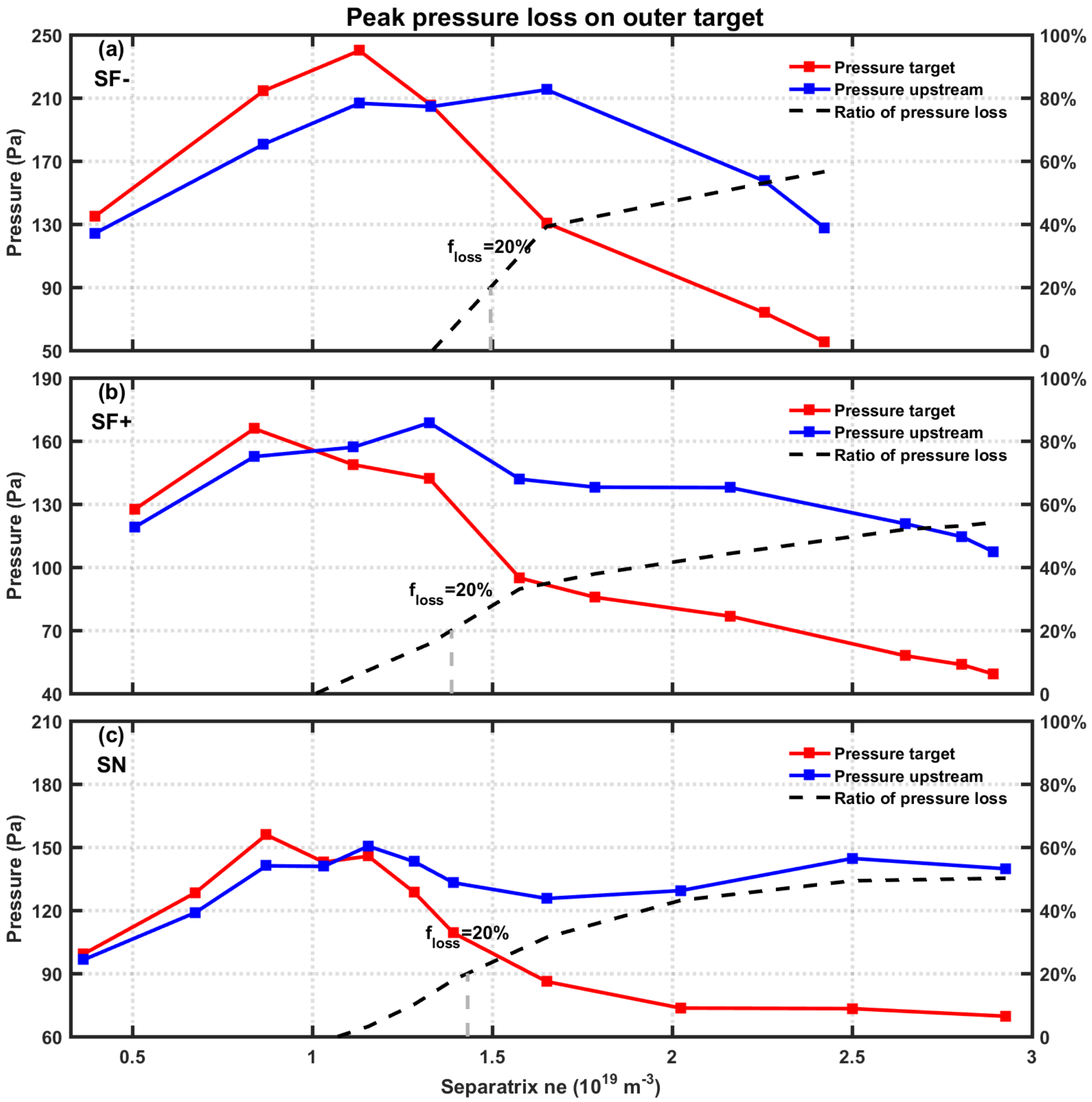

figure 15. Comparison of the peak pressure on target (red line) and the upstream pressure (blue line) at the same magnetic tube in function of the upstream density, define the detachment as a more than 20% loss. The pressure corresponds to the left y-axis, $P = n_e(T_e + T_i)(1 + M^2)$. The black dash line represents the ratio of pressure loss between target and upstream, corresponding to the right y-axis.

As shown in figure 15, if we define the significant pressure loss as a more than 20% ratio of loss, the detachment thresholds of SF- is a little higher than SN and SF-, $n_e{\sim}1.5 \times 10^{19}\ m^{-3}$ for SF-, $n_e{\sim}1.4 \times 10^{19}\ m^{-3}$ for SN/SF+, $\Delta_{nu} < 10\%$. But SF- has a higher performance after detachment. For a detachment plasma $n_e{\sim}2 \times 10^{19}\ m^{-3}$, the pressure loss $f_{loss}{\sim}40\%$ for SN and SF+, $f_{loss}{\sim}48\%$ for SF-. The pressure loss of SF- rises faster with the separatrix density, it reveals a higher degree of detachment for SF- plasma. There is no indication of a reduced detachment threshold with the second X-point near the target.

5.4 Impact on detachment window

The detachment window is defined as the density interval over which the radiation front moves from target to X-point. The narrower this window, the more sensitive detachment state is with respect to density (and possibly other actuators) [26]. In the following, we investigate how this density window is affected by the divertor geometry. The evolution of radiation profiles during the detachment process for three configurations is shown in figure 16. Comparison between SN and SF+ cases, figure 16(d), the detachment window increase from $\Delta_{nu}\approx 0.7\times 10^{19}m^{-3}$ for SN, to $\Delta_{nu}\approx 1\times 10^{19}m^{-3}$ for SF+, for a change of parallel connection length from $L_{\parallel,\mathrm{SN}}\approx 23\ \ m$ to $L_{\parallel,\mathrm{SF+}}\approx 120\ \ m$. It suggests an increase of the density window with parallel connection length. On the other hand, the SF- configuration has a narrowest detachment window $\Delta_{nu}\approx 0.6\times 10^{19}m^{-3}$ and a parallel connection length of $L_{\parallel,\mathrm{SF-}}\approx 70$, which seems to contradict the later suggestion. In reality the radiation front moves not only toward the X-point but also across flux surfaces (fig16). A simple parametrization with a local connection length close to separatrix may not be a robust figure of merit.

The start of the radiation front movement occurs at slightly lower densities than the roll-over in ion flux and the pressure loss. The SN and SF+ configurations achieve radiation detachment onset at a lower upstream density $\mathrm{n_e}{\sim}0.97\times 10^{19}\ \mathrm{m}^{-3}$ for SN, $\mathrm{n_e}{\sim}0.9\times 10^{19}\ \mathrm{m}^{-3}$ for SF+ and then SF- plasma start to detach at $\mathrm{n_e}{\sim}1.15\times 10^{19}\ \mathrm{m}^{-3}$ for SF-. This result can also be considered consistent with local particle detachment onset in terms of parallel ion flux roll-over on strike point and peak regime, as shown in figure 10.

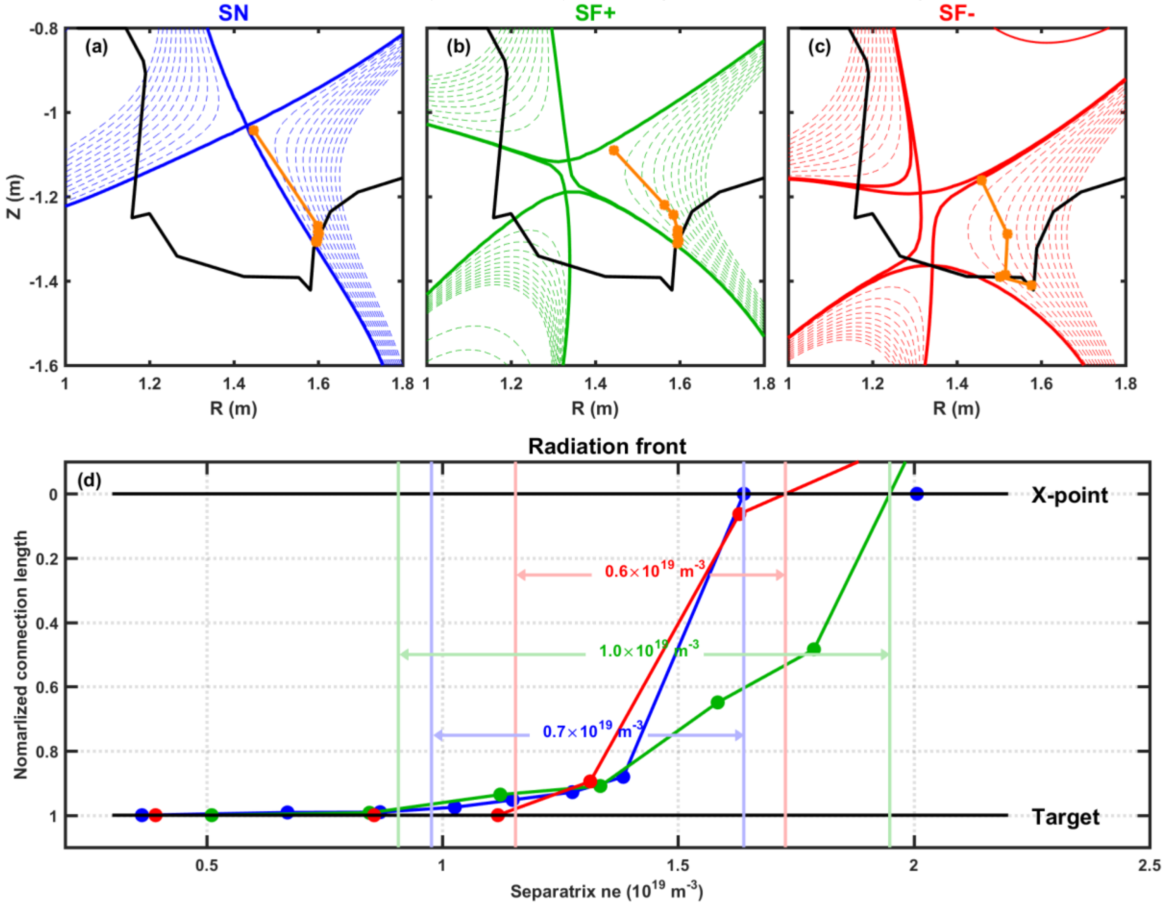

Figure 16. (a)–(c) Flux surface in the divertor volume for three configurations. The orange dot represents the position of radiation peak during the density ramp simulations. These three

cases correspond to the evolution of radiation front shown below, with the same color. (d) Position of the front edge along the outer leg as a function of separatrix density.

Summary and conclusions

The impact of specific aspects of the magnetic and wall geometry on divertor detachment process is studied using SOLEDG2D-EIRENE simulations for HL-2M configurations in Ohmic density ramp with pure deuterium plasma. Three different divertor magnetic configurations are investigated, looking at the impact of connection length and flux expansion on detachment properties. Connection length increases by approximately a factor 6 from SN to SF+ configurations while flux expansion f_x at the outer target is varied by a factor 10 for SF- configuration with respect to SN one.

Some characteristics of the outer target detachment are assessed in these simulations. As a measure of the detachment threshold, we take here the upstream plasma density corresponding at the roll over in the ion particle flux on the outer target: the roll over of integrated ion flux indicates the threshold of integrated detachment and the roll over of peak ion flux indicates the threshold of partial detachment. The Degree Of Detachment is computed and used to estimate the level of detachment. The density range estimated from the instant when the radiation front starts to detach from target and when it arrives at the X-point. Detachment control can benefit from a broader upstream density window.

Comparing the detachment process for SN, SF+ and SF- configurations, we find that SN and SF+ plasma always have similar threshold of detachment, $\Delta_{nu} < 10\%$, in terms of all detachment process: power dissipation, momentum and particle flux losses. The SF- achieve integral particle detachment at a lower upstream density, $n_e \sim 1.6 \times 10^{19}\ m^{-3}$, while $n_e \sim 2.2 \times 10^{19}\ m^{-3}$ for $\mathrm{SF+}$ and $n_e \sim 2.5 \times 10^{19}\ m^{-3}$ for SN. However, SF- has a higher threshold for local detachment (separatrix $n_e \sim 1.6 \times 10^{19}\ m^{-3}$) compared to the SN & SF+ where plasma local detachment onset is observed at $n_e \sim 1.3 \times 10^{19}\ m^{-3}$.

The comparison of detachment threshold for these three configurations does not show a clear dependence on the connection length, as one could expect from 2-point model considerations. It seems that the penetration of neutrals and its dependence on geometrical aspects like vertical vs horizontal plate configuration as well as close vs open divertor could explain at least partially these behaviors. More specifically closure divertor for SF- and the vertical target plate for SN/SF+ reduce the threshold of integral and local detachment respectively, consistent with the C-Mod [33], ASDEX-Upgrade [34] and JT-60U [35] experiment results. On the other side it seems that connection length can explain why the SF+ configuration has a wider detachment window $\Delta_{nu} \approx 1 \times 10^{19} m^{-3}$, with respect to SN configuration where $\Delta_{nu} \approx 0.7 \times 10^{19} m^{-3}$ and SF- where $\Delta_{nu} \approx 0.6 \times 10^{19} m^{-3}$. This comparison reveals that the detachment window increases with connection length. On the other hand, the SF- plasma has a higher degree of detachment both in particle and momentum detachment.

The simulations and analysis presented here constitute a basis for more detailed studies of geometrical dependences of detachment on HL-2M configurations and even CFETR future reactor device. In the future, the H-mode plasma will be simulated, and the light impurities will be injected to study how the present picture changes under these conditions. To go further, the simulations of alternative configurations with different geometry parameters and second X-point positions are needed, to find a clearly, quantitative dependence of detachment behavior on geometrical parameters e.g. f_x, α, $L_\parallel$, R_t. Moreover, we will investigate the additional effect of the second X-point in the main SOL regime for the SF-configuration, for example, power repartition between active strike points.

It should be noticed that the electrostatic potential, grad B and ExB drifts can have a strong impact on particle and heat flux recirculation patterns in the divertor region, even if it is not completely clear if their role is always dominant or not. However, in this paper we have started from a detailed study without drifts allowing us to a better comprehension of the effect of magnetic and wall geometry disentangling these aspects from the drifts impact. We plan future studies with the activation of drifts to determine their impact in these configurations.

Acknowledgements

This work was granted access to the HPC resources of Aix-Marseille University financed by the project Equip@Meso (ANR-10-EQPX-29-01). The project leading to this publication (TOP project) has received funding from Excellence Initiative of Aix-Marseille University- A*MIDEX, a french ‘Investissements d’Avenir’ programme. This work has been carried out within the framework of the EUROfusion Consortium and has received funding from the Euratom research and training programme 2014-2018 under grant agreement No 633053. The views and opinions expressed herein do not necessarily reflect those of the European Commission

References

[1] H. Bufferand *et al*, 2015 Nucl. Fusion **55,** 053025
[2] Janeschitz G, Borrass K, Federici G, Igikhanov Y et al, 1995 J. Nucl Mater. 220-222, 73
[3] A Loarte et al. Progress in the ITER Physics Basis Chapter 4: Power and particle control 2007 Nucl. Fusion 47 S203
[4] A W Leonard. 2018 Plasma Phys. Control. Fusion 60 044001
[5] Loarte A, Monk R D and Martin-Solis J R 1998 Nucl. Fusion 38 331
[6] C. Theiler, et al 2017 Nucl. Fusion 57 072008
[7] H. Reimerdes, et al 2017 Nucl. Fusion 57 126007
[8] Kallenbach A, Dux R, Mertens V and Gruber O 1995 Nucl. Fusion 35 1231
[9] Petrie T W, Buchenauer D, Hill D N and Klepper C 1992 J. Nucl. Mater. 196–198 848
[10] Hosogane N, Asakura N, Kubo H and Itami K 1992 J. Nucl. Mater. 196–198 750
[11] Lipschultz B, Goetz J and LaBombard B 1995 J. Nucl. Mater. 220–222 50
[12] Kallenbach A et al 2015 Nucl. Fusion 55 053026
[13] Ryutov D.D. 2007 Phys. Plasmas 14 064502
[14] O Pan et al 2018 Plasma Phys. Control. Fusion 60 085005
[15] Covele B et al 2017 Nucl. Fusion 57 086017
[16] LaBombard B. et al 2015 Nucl. Fusion 55 053020
[17] Kotschenreuther M., Valanju P., Covele B. and Mahajan S. 2013 Phys. Plasmas 20 102507
[18] Lipschultz B., Parra F.I. and Hutchinson I.H. 2016 Nucl. Fusion 56 056007
[19] V. Rozhansky et al, Nucl. Fusion 49 (2009) 025007

[20] X. Bonnin, W. Dekeyser, R. Pitts, D. Coster, S. Voskoboynikov and S. Wiesen, Plasma Fusion Res. 11 (2016) 1403102
[21] Porter G. D., Petrie T. W., Rognlien T. D., and Rensink M. E. Physics of Plasmas, 2010, 17 112501
[22] Chankin A. V.et al, Plasma Phys. Control. Fusion 59 045012
[23] R. Mao et al 2018 Contrib. Plasma Phys. 2018, 58 :781-790
[24] G. Ciraolo et al 2017, Nucl Mat. and Energy, 12,187-192
[25] E. Joffrin et al 2017, Nucl. Fusion 57, 086025
[26] A Gallo et al 2018 Plasma Phys. Control. Fusion 60 014007
[27] KJeško et al 2018 Plasma Phys. Control. Fusion 60 125009
[28] X.R. Duan et al 2017 Nucl. Fusion 57, 102013
[29] Moulton at al 2017 Plasma Phys. Control. Fusion 59 065011
[30] RA Pitts, S Carpentier, F Escourbiac, et al Journal of Nuclear Materials 415(1), S957-S964
[31] L. Isoardi et al Journal of Computational Physics, Volume 229, 2010, pp. 2220-2235
[32] B. Bensiali, G. Chiavassa, J. Liandrat, Applied Numerical Mathematics, Volume 96, 2015, pp. 134-152
[33] Loarte A. et al 2001 Plasma Phys. Control. Fusion 43 R183
[34] Schneider R, Bosch H S, Coster D and Fuchs J C 1999 J. Nucl. Mater. 266–269 175
[35] Asakura N, Hosogane N, Itami K and Sakasai A 1999 J. Nucl. Mater. 266–269 182
[36] T. Eich et al., Physical Review Letters 107 (2011), 215001